Thin Solid Films 522 (2012) 473–479

Contents lists available at SciVerse ScienceDirect

Thin Solid Films

journal homepage: www.elsevier.com/locate/tsf

Fabrication of metallic nanoparticles by spinodal dewetting of thin films: A high-throughput approach

William D. Michalak [a,b], James B. Miller [a,b], Cem Yolcu [c], Andrew J. Gellman [a,b,*]

[a] U.S. Department of Energy, National Energy Technology Laboratory, Pittsburgh, PA 15262, USA
[b] Department of Chemical Engineering, Carnegie Mellon University, Pittsburgh, PA 15213, USA
[c] Department of Physics, Carnegie Mellon University, Pittsburgh, PA 15213, USA

ARTICLE INFO

Article history:
Received 10 April 2012
Received in revised form 7 July 2012
Accepted 12 July 2012
Available online 20 July 2012

Keywords:
Spinodal dewetting
Metal nanoparticles
High-throughput
Structural gradient
Thin films
Palladium
Silicon nitride

ABSTRACT

Metal nanoparticles on structured supports are used in a variety of technological applications including biosensing, energy harvesting, and electronics. In every case, the functions and properties of the metallic nanostructures depend on both their composition and structure (i.e. size, shape, and spatial distribution). Among the challenges to the development of metal nanoparticles for these applications is the characterization of relationships between their structure and their functional properties over multiple structural degrees of freedom spanning a large range of values. In this work, a method for creating a morphological gradient of metal nanoparticles on a substrate is described. The approach, suited for high-throughput fabrication and characterization, is based on spinodal dewetting of a metallic thin film from its substrate. Through control of initial film thickness, anneal temperature, and anneal time, spinodal dewetting results in supported nanoparticles with well-defined and controlled structure. The approach is demonstrated through its application to preparation of Pd nanoparticles on a silicon nitride substrate. The morphologies of the particles were characterized by scanning electron and atomic force microscopies. Free energy-based stability and topological analyses were used to confirm the dewetting mechanism. In addition, the stability theory provides a connection to the thermophysical properties of the resulting nanoparticle array. The dewetting approach is general to any metal/support system and provides an alternative, inexpensive, and robust means to rapidly create metal nanostructures with control of morphology. It shows promise for large scale production of metal nanoparticles structures, as well as understanding basic stability properties of thin metal films.

1. Introduction

Many technologically significant systems benefit from the unique properties of nano- and micro-sized, metal structures. Photonic [1], optoelectronic [2,3], microelectronic [4], information storage [5], and biosensing [6,7] devices are based on nanostructured metallic components with functions and properties that depend on their composition, structure, size, shape, and spatial distribution. For example, the efficiency and material requirements of solar radiation conversion by photovoltaic cells are improved by creating structured, plasmon-active metal clusters (e.g. Au, Ag, Cu, and Al) on the semiconductor surface to guide and confine incident sunlight [8,9]. Heterogeneous catalysts for many chemical conversions use metallic nanoparticles dispersed on solid supports [10–12]. Nanoparticles are used to improve the sensitivity of biosensors that detect molecular binding events and changes in molecular conformation [7]. In every instance, the morphology (i.e. shape and size) and topography (i.e. spatial distribution) of the metal particles have been shown to be an important determinant of the material's properties and performance.

Understanding and optimizing nanoparticle systems require that they be prepared and characterized over broad regions of structure space (morphology and topography). The high-throughput/combinatorial approaches that are widely used in biotechnology [7,13,14] also offer opportunities for accelerated determination of structure–property relationships. However, with the exception of polymeric systems [15], these approaches are not commonly applied in the physical and material sciences due to the limitations of the methods used to fabricate solid-state materials. For this reason, high-throughput study of solid-state systems focuses almost exclusively on spanning compositional space [16,17].

The common methods used to fabricate nano- and micro-meter sized metal particles – high-temperature vapor deposition, lithography-based vapor deposition, and colloidal chemical synthesis – are poorly suited for rapid generation, characterization, and optimization of materials over broad structural degrees of freedom. In this work, a method is described for creating a structural gradient of nano- to micro- meter sized metal particles on a solid support for high-throughput studies. The approach involves controlled dewetting of a continuous thin metal film prepared with a thickness gradient on a single substrate.

---

[*] Corresponding author. Tel.: +1 412 268 3848; fax: +1 412 268 7139.
E-mail address: gellman@cmu.edu (A.J. Gellman).

0040-6090/$ – see front matter © 2012 Elsevier B.V. All rights reserved.
doi:10.1016/j.tsf.2012.07.041

Four modes for dewetting of thin films are described in the literature: (1) grain boundary mediated dewetting caused by thermal grooving [18,19]; (2) heterogeneous nucleation of holes caused by defects or foreign particles on the surface; (3) thermal nucleation of holes caused by temperature gradients and hotspots on the surface; and (4) spinodal dewetting [20–26]. The first three modes are nucleation-dominated mechanisms, whereas spinodal dewetting is driven by thermodynamic system instability. The different modes can be distinguished by their geometrical signatures [26] and the onset time for the dewetting process: thermal nucleation and thermal grooving have nucleated holes that are randomly distributed in location and time of appearance, whereas holes formed by both heterogeneous nucleation and spinodal dewetting appear at early stages of the dewetting process, can have non-random size distributions, and can display ordered spatial distributions.

Spinodal dewetting is a promising route for the creation of nanoscale metal structures because it has the advantages of repeatable and self-organized assembly of nanoparticles with predictable sizes, shapes, and inter-particle distances that are, in principle, determined only by the thermophysical material properties of the substrate/film combination and the initial thickness of the film, h_0. Structures accessible through spinodal dewetting include hemispherical droplets, irregular asymmetric particles, connected polygons, randomly oriented ridge-like structures, and plateaus of continuous film with dispersed holes [22,25,27–30].

Over the last 15 years, a number of reports have suggested that spinodal dewetting is dominant in the initial stages of thin metal film breakup induced by localized irradiation with nanosecond laser pulses, whereby the metal film is heated to its melting point (e.g. Au [27,28], Co [29], Ni [27,28], Fe [29], Cu [27,28], Ag [22] on SiO_2; and Pt on Si [27,30]). These previous efforts assert that the transition to a liquid phase at high temperatures – achieved by pulsed-laser heating – is necessary to induce spinodal dewetting of the metallic thin films.

In this work, we show that a liquid state is not a prerequisite for spinodal dewetting. We show that the spinodal dewetting mechanism is independent of the material phase based on a free energy-based theoretical description and experimental observations, whereby we induce spinodal dewetting of Pd from a silicon nitride (SiN) surface by thermal annealing of the substrate/film system at temperatures well below the bulk metal melting point.

Pulsed-laser heating is limited to creating dewetted structures over very small spatial domains and results in temperature gradients perpendicular to the substrate. Our approach differs in that we induce spinodal dewetting across the entire substrate through uniform conductive heating of the entire substrate/film system. We can, therefore, deposit films with regions of different local initial thickness on a single substrate and prepare a diverse set of microstructures under identical external conditions. This thickness gradient allows the creation of a materials library that contains a diverse set of structures on a single compact substrate in manner similar to that described by Meredith et al. [15]. We use topological analyses of the structural gradients to confirm that the metal structures that we observe result from spinodal dewetting.

2. Methods

2.1. Experimental techniques

A 150 nm thick SiN film was prepared by r.f. magnetron sputtering on a Si(100) wafer with a 1 μm oxide surface layer. A thin layer of Ta was deposited on the back side of the Si(100) wafer to improve thermal conduction between the Mo mounting support and sample. The wafer was cut to 1 cm^2 squares and the substrate was cleaned by sonication in ethanol for 10 min followed by immersion in 1:3 H_2O_2:H_2SO_4 (piranha solution) for 10 min, a deionized water rinse, and final drying in N_2. The substrate was mounted on a flat polished, 0.5 mm × 1 cm^2 Mo plate prior to placement of the substrate in an ultra-high vacuum chamber for Pd deposition. The sample was heated by conductive transfer from the resistively heated Mo support which retained the sample by a spring-tension clamp. The temperature of the holder was monitored with a K-type thermocouple that was spot welded to the backside of the Mo plate. The Mo plate was mounted by Mo wires to electrically isolated copper plates which were attached to a hollow steel bar that acted as a heat sink.

The chemical composition and surface cleanliness of the SiN surface before Pd deposition were verified using X-ray photoelectron spectroscopy (XPS). The XPS system was composed of a hemispherical energy analyzer (VG, CLAM-2) and an X-ray source (Specs, XRC-1000). Pd was deposited onto the SiN at a constant temperature of ~340 K at a rate of 1 nm/min using a Knudsen effusion source (Createc-Fischer GmbH, HTC). The deposition rate was calibrated with a quartz crystal microbalance (QCM, Maxtek, Inc., TM-350). Multiple thicknesses were deposited on the sample using a steel mask, which was positioned immediately above the substrate and moved by 1 mm every 5 min during film deposition. Pd films of eight thicknesses were formed across the sample in bands with ~1 mm widths and ~5 nm height increments. Dewetting of the Pd film was initiated by heating the sample and support to 800 K for 1000 s. The sample was cooled under vacuum conditions to preserve the structures that were formed upon dewetting. After cooling, the sample was removed from the UHV chamber for analysis of the film structure.

The morphology of the dewetting films was studied using atomic force microscopy (AFM, Digital Instruments, Multimode with Nanoscope v5.18 software) in tapping mode with a silicon nitride tip (Budget Sensors Tap-300). The Pd morphology with respect to the bare SiN was measured by profilometry at each step in the thickness gradient by traversing across a groove which was created perpendicular to the Pd steps (c.f. Fig. 1b). The topography was imaged using AFM and scanning electron microscopies (SEM, FEI Quanta (20 keV)). Contact angles were also measured by SEM-imaging of sample cross-sections. A clean cross section was created by taking advantage of the crystalline nature of the Si wafer — a break was initiated by scratching the backside of the wafer with a diamond scribe to minimize damage to the Pd film.

2.2. Pattern analysis

The two dimensional Minkowski functionals, $M_{\nu=0,\,1,\,2}$, are related to the familiar geometric quantities of covered area, F, boundary length, U, and Euler characteristic, χ, which is the number difference of connected domains and holes (by definition an entirely black/white image has a $\chi=0$) [31,32]. The respective Minkowski functionals are given as $M_0=F$, $M_1=(1/2\pi)\,U$, and $M_2=(1/\pi)\,\chi$. We calculated the Minkowski functionals using the marching square algorithm described by Mantz et al. [32]. The algorithm requires that a gray scale image be divided into 256 binary (black and white) images whereby each image corresponds to a threshold pixel value ranging from 0 to 255; all pixels that are below the threshold are set to white and those above are set to black. This threshold-based subdivision generates 256 isoheight planes which, as a collection, represent the 3-D morphology.

Spatial correlation analysis, including calculations of the two dimensional Fourier transforms and radial power spectra of the SEM images, was performed using Gwyddion SPM and Imaging Metrology SPIP software.

2.3. Parameter estimation

We estimated the most probable values for the A, h_c, and γ using a Monte Carlo sampling routine. The uncertainty was measured using a bootstrapping regression analysis over the parameters in log-space. With this approach, the uncertainty, σ_i, of parameter φ_i, is given by the expression $\sigma_i = \sqrt{\overline{\varphi_i^2} - \bar{\varphi}_i^2}$. Notice that there is no factor of $1/(N-1)$ because that would imply the uncertainty could be decreased by resampling the resampled data. We generated the 95% confidence limits

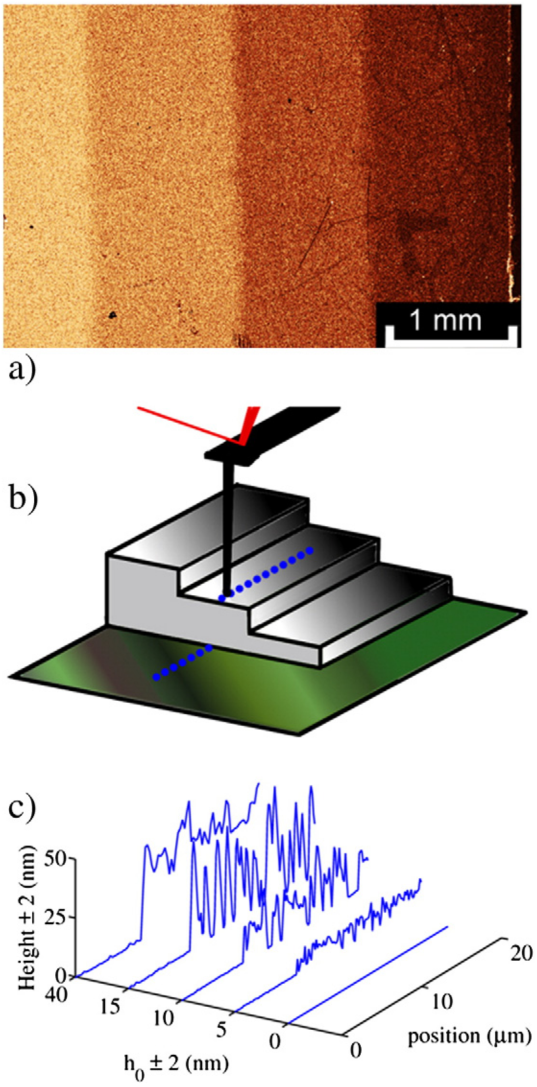

Fig. 1. (a) A wide-field SEM image of the first four Pd steps (5, 10, 15, 20 nm) on the SiN substrate. (b) Schematic of the step structure of the Pd thin film thickness gradient and the use of AFM to measure the height relative to the substrate. The dotted blue line corresponds to a single linescan across a bare region of the SiN substrate and onto the Pd film. (c) AFM linescans for five different initial thicknesses, h_0, where h_0 and the measured height are in units of nm, and the position along the linescan is in units of μm.

using Monte Carlo error propagation methods, which assumed normal probability distributions for the dependent variables.

3. Results

A Pd thin film was vapor deposited onto a 1 cm × 1 cm × by 150 nm thick SiN substrate as described in the Methods section. The Pd thin film was prepared with a lateral thickness gradient consisting of 1 mm wide bands with initial thicknesses, h_0, spanning the range 5–40 nm in 5 nm increments. Dewetting of the precursor film was induced by uniform heating of the sample at 800 K for 1000 s under a vacuum of 1.33×10^{-6} Pa. A wide field SEM of the four thinnest films ($h_0 = 5$, 10, 15, 20 nm) following the heat treatment is shown in Fig. 1a. The figure shows well-defined steps via the color contrast, but the resolution at this magnification does not reveal structural differences between the films at each thickness.

To demonstrate the variations in morphology of the annealed films with increasing h_0, we measured the height and morphology of the dewetted structures by AFM imaging across a groove on the sample (illustrated in Fig. 1b). Fig. 1c shows single line-scans for five different initial thicknesses: $h_0 = 0$, 5, 10, 15, 40 nm. These profiles demonstrate the differences in Pd structures with increasing h_0. The films show clear evidence of dewetting for initial thicknesses of $h_0 = 5$–15 nm, but have not dewetted from the substrate at $h_0 =$ 40 nm. Comparison of the film morphologies within this simple structural gradient provides immediate clues about the dewetting mode of the thin metal film. The distribution of the features and similarity in size in the 15 nm profile in Fig. 1c suggests that thermal nucleation and thermal grooving are unlikely; neither mode results in dewetted films with regular spacing between features (order) or similar sizes. Because the SiN surface is relatively smooth (rms roughness of ~0.2 nm,) and was carefully cleaned prior to film deposition (see Methods: Experimental), spatial heterogeneity on the surface – and, thus, heterogeneous nucleation – is unlikely.

Comparison of the measured heights at each value of h_0 provides qualitative evidence of a spinodal dewetting mechanism. Fig. 1c shows that the difference between height minima and maxima varies considerably with h_0. These differences are characteristic of spinodal dewetting, during which capillary surface waves spontaneously amplify so that the film separates into regions of h equal to the equilibrium thickness (h_c, i.e. the thickness of a coherent film that would remain on the surface after dewetting takes place) and $h = \infty$ [33]. Because the volume of the film remains conserved, local thinning is compensated by thickening in other regions [34]. This behavior is similar to spinodal decomposition of a metastable binary solution where a finite fluctuation renders the solution unstable and causes an immediate phase separation. The phase separation results in compositional modulations that have well-defined spacing between the peaks in the modulations [35]. For the Pd profile at $h_0 < 20$ nm, the height limits in the dewetted film extend from $h \approx 0$ to $h > h_0$ (sometimes much greater) — this is analogous to compositional modulations observed in spinodal decomposition, and provides evidence of spinodal dewetting. In contrast, the profile of the annealed film with $h_0 = 40$ nm (representative of the morphology for all films with $h_0 > 20$ nm) fluctuates around h_0 without exposing the substrate. At the higher values of h_0 (illustrated by the 40 nm profile) the profile does not suggest a morphology that is characteristic of spinodal dewetting because time scale for film rupture ($\propto h_0^5$) [20,23,24,36–38] is long compared to the annealing period and, therefore, the surface waves have not yet reached amplitudes equivalent to h_0. This is why the maximum heights of the features in the 15 nm and 40 nm films are nearly equal.

The topographies of dewetted metal films can be characterized by scanning electron microscopy (SEM) or atomic force microscopy (AFM). SEM images of regions with $h_0 = 5$, 10, and 20 nm are shown in Fig. 2 with two view fields (wide: left; narrow: center). The different in-plane length scales (labeled in the bottom left corners) are used to reveal the details of the structures. The three regions also show recognizably distinct structures that are complementary to the line-scans shown in Fig. 1c and illustrate some structures predicted by spinodal dewetting [22,25,27–30]. These images represent snapshots of the progression of structures formed as the dewetting film evolves in time [39]: coherent film; film with scattered holes ($h_0 = 20$ nm); buildup of holes until adjacent holes create polygons; breakup of polygons into interconnected ridge structures ($h_0 = 10$ nm); and finally, individual cluster units ($h_0 = 5$ nm). A significant point is that the structures shown are not unique to the particular initial thickness — all structures can be achieved for any given value of h_0. It is possible to obtain patterns with almost any length scale and shape in a repeatable and self-organized manner by simply adjusting the annealing time. These images illustrate a small sample of possible accessible structures.

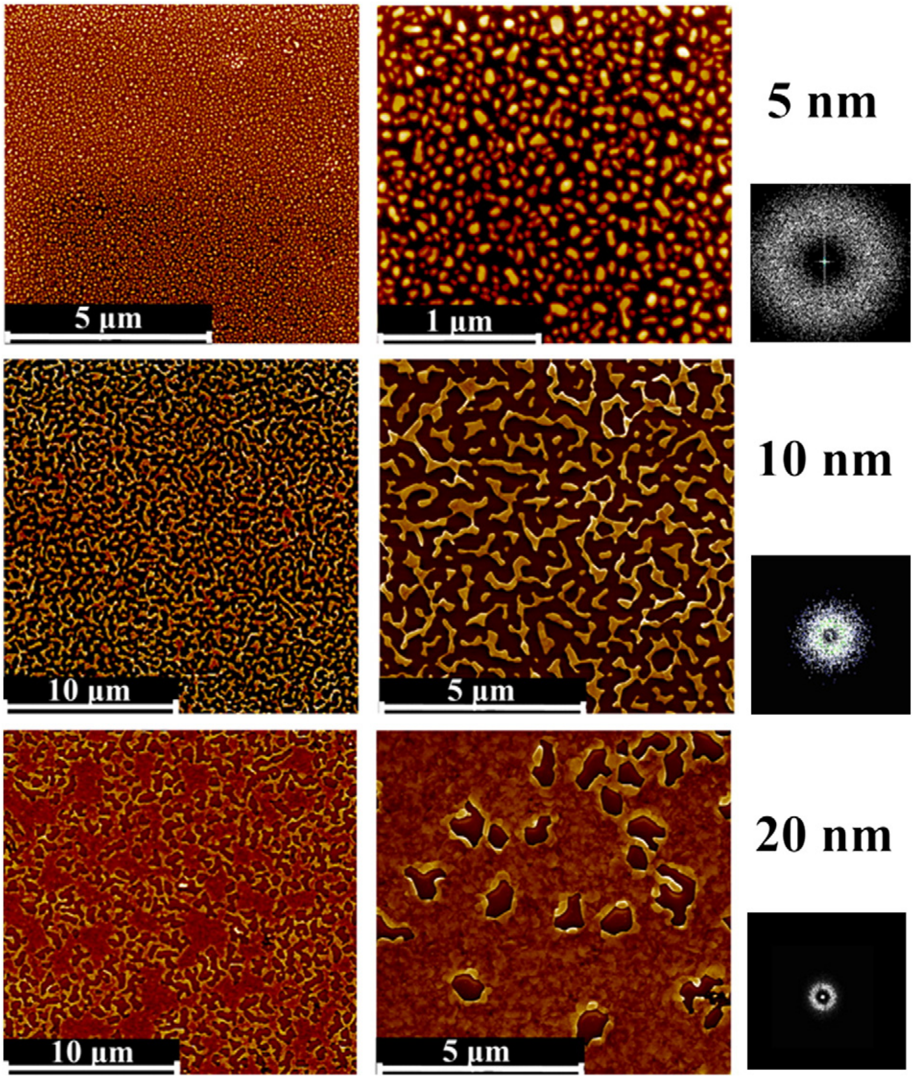

Fig. 2. SEM images of the topographies of dewetted films with initial thickness of $h_0 = 5$, 10, and 20 ± 2 nm. Radial power spectrum distributions (RPS) for each image are shown in the right column. The radius of the RPS decreases with increasing initial thickness, quantifying the increase in the mean spacing between features in the images.

Beyond visual inspection, we can quantitatively confirm the spinodal dewetting mechanism through characterization with Minkowski functionals, which identify structures that exhibit properties of Gaussian random fields [31,32], and with methods that measure spatial frequencies of the film structure. Minkowski functionals have been used to model many geometrical features observed in physical data such as cosmic background radiation, capillary waves at fluid interfaces, spinodal decomposition, and spinodal dewetting [31,32]; each example has features consistent with a Gaussian random-field (GRF) model. Minkowski functionals, M_ν, are integral geometry measures of the covered area (M_0), boundary length (M_1) and the Euler characteristic (M_2); the latter describes a purely topological feature of the structure without using a metric, but can be associated with connectivity of shapes [32] (see Methods: Pattern analysis). Fig. 3a displays normalized M_1 (black/left axis) and M_2 (red/right axis) versus M_0 for $h_0 = 5$ (○), 10 (□), 15 (x), 20 (◊), 25 (⁎), and 30 (•) nm, and the GRF model (solid line). The Minkowski functionals in Fig. 3a show that the dewetting behavior of Pd on SiN displays features that are characteristic of the GRF model. This suggests that the process occurs by spinodal dewetting.

We can further support the spinodal dewetting behavior of the metallic film and estimate some of its thermophysical properties by studying the spatial frequencies of the film structures across all topographies measured in the thickness gradient (such as those shown in Fig. 3). The existence of unique spatial frequencies in a dewetted/deformed film following a spinodal instability is well-known for liquids, polymers, and metals. A theoretical framework based on liquids is established [20,23,24,33,36,38,39]. In many cases, the theories begin with an equation of motion such as Navier–Stokes. However, prediction of spinodal instabilities does not require hydrodynamics [24]. In fact, the phase of the material is irrelevant.

Consider the film profile of height $h(\vec{\chi},t)$ above point $\vec{\chi} = (x,y)$ on a substrate. The total free energy of a supported, defect-free, thin film on an inert substrate is

$$F(t) = \int dxdy\left[\gamma\sqrt{1+(\nabla h(\vec{\chi},t))^2} + G\left(h\left(\vec{\chi},t\right)\right)\right] \qquad (1)$$

where the interfacial potential, G, is the energy density per unit area required to bring two interfaces (film-substrate and film-vacuum) from infinity to a certain distance, h. The quantity γ is the surface tension between the film surface and vacuum and t is time. To determine

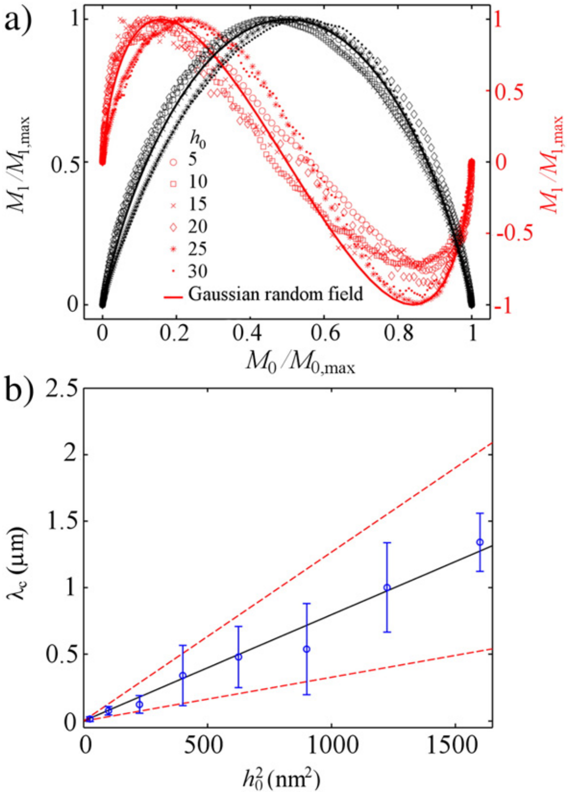

Fig. 3. a) Normalized Minkowski functionals M_1 (black/left axis) and M_2 (red/right axis) versus M_0 for $h_0 = 5$ (○), 10 (□), 15 (x), 20 (◊), 25 (⁎), and 30 (•) nm and the expectation for the Gaussian random-field model. b) Characteristic wavelength λ_c of dewetted Pd films with increasing initial thickness, h_0. A linear relationship (c.f. Eq. 5) between λ_c and h_0^2 corroborates the spinodal dewetting mechanism. The circles represent the experimental data with 95% confidence error bars and the solid black line represents the most probable fit with the 95% confidence intervals (dotted red lines) based on the model Eq. (5).

the fate of the film given a thermal perturbation, we can perform linear stability analysis by introducing a small deformation of the film, $u(\vec{x},t)$, around h_0, so that $h = h_0 + u$. Following substitution of h into Eq. (1), the entire expression can be expanded to the lowest nontrivial order (i.e. quadratic) and the free energy of the system can be re-expressed as

$$F(t) = \frac{1}{2}\int dxdy\left[\gamma(\nabla u)^2 + G''(h_0)u^2\right] \tag{2}$$

where the double prime indicates the second derivative. Expressing u as a superposition of Fourier modes, with wave vector $\vec{k}$ and amplitude, $u_{\vec{k}}(t)$, as

$$u(\vec{x},t) = \sum_{\vec{k}} u_{\vec{k}}(t)e^{i\vec{x}\cdot\vec{k}}, \tag{3}$$

the free energy can now be rewritten as a sum over independent fluctuation modes as

$$F(t) = \pi\sum_{\vec{k}}\left[\gamma k^2 + G''(h_0)\right]\left|u_{\vec{k}}(t)\right|^2 =: \sum_{\vec{k}} F_{\vec{k}}(t). \tag{4}$$

where $k = |\vec{k}|$.

A dewetting film is characterized by the increasing amplitude of its surface undulations, i.e. $d|u_{\vec{k}}(t)|^2/dt > 0$. However, this growth of the undulations is only spontaneous provided that it also corresponds to a decrease in the free energy of its associated mode, i.e. $dF(t)/dt < 0$. According to Eq. (4), the two conditions can only hold simultaneously if $\gamma k^2 + G''(h_0) < 0$. The inequality indicates that spontaneous dewetting may occur only when $G''(h_0)$ is negative and k is not too large (note that γk^2 is always positive). This means that both stable (decaying) and unstable (growing) modes will be present. The unstable modes for a given h_0 can be determined by rearranging the inequality as

$$\lambda > 2\pi\sqrt{\frac{-\gamma}{G''(h_0)}} =: \lambda_c \tag{5}$$

where we define $\lambda = 2\pi/k$. The characteristic wavelength, λ_c, specifies the modes of shortest wavelength that have a chance to persist as the interface evolves. In fact, under certain assumptions about the phase and dynamics of the material, these "characteristic modes" are believed to grow faster than all other unstable modes [20,21,24,25,27–29,33,36,39,40]. Unlike previous derivations of Eq. (5), this does not require parameters, such as viscosity, that depend on the phase of the material because the equations of material transport are irrelevant as far as the onset of instability is concerned.

To use Eq. (5) to correlate λ_c to our experimental observations we must define G. For thin films, both non-retarded dispersion and short-range Born repulsion forces are commonly included and the effects of gravity are assumed negligible. Previous reports have also included electrostatic effects, which would be caused by differences in the work functions of the materials [41]. Electrostatic forces are likely to be negligible at the Pd/SiN interface due to the electronic screening in metals. In addition, there is no induced electric field between the substrate and vacuum. We would only consider an induced electric field, if the vacuum was replaced by a conductive medium. We define G as

$$G(h) = \frac{A}{2h^2} - \frac{Ah_c^6}{24h^8} \tag{6}$$

where A is the Hamaker constant. This equation represents the thin-film equivalent of the Lennard-Jones potential with the non-retarded dispersion and short-range Born repulsion forces, respectively [23,37,42]. In other words, a film with $h \le h_c$ is stable and does not dewet. This thickness is also related to the contact angle of the dewetted film on the substrate by

$$G(h_c)/\gamma = \cos\theta - 1 \tag{7}$$

where θ is the contact angle of the film with respect to the substrate [37,43]. Inserting Eq. (6) into Eq. (5) yields an approximation to λ_c as

$$\lambda_c = 2\pi\left(-\frac{\gamma}{G''(h_0)}\right)^{1/2} = 2\pi\left(-\frac{\gamma h_0^{10}}{3Ah_0^6 - 3Ah_c^6}\right)^{1/2} \approx 2\pi\left(-\frac{\gamma}{3A}\right)^{1/2} h_0^2 \tag{8}$$

where $1 \gg \left({}^{h_c}/_{h_0}\right)^6$.

Observation of a linear relationship between λ_c and h_0^2 suggested by Eq. (8) provides evidence for a spinodal dewetting mechanism. This relationship deviates when coarsening (Oswalt ripening) becomes prominent at later stages in time. We obtained estimates of λ_c from radial power spectra (RPS) of the SEM topographies (Fig. 2) by means of a two-dimensional Fourier transform. The RPSs of the wide field images are shown in the panels on the right-side of Fig. 3. The RPS distributions display an annulus whose radius decreases with increasing h_0; this corresponds to an increase of λ_c with h_0. The linear correlation between λ_c and h_0^2 is shown in Fig. 2b – corroborating the spinodal dewetting hypothesis – where circles represent the experimental data with 95% confidence limits and the solid line represents the most probable fit with its 95% confidence intervals (dotted lines). Because the repulsive term has negligible impact in Eq. (8), we must use an alternate approach to identify h_c and fully define the intermolecular potential. Experimentally measured contact angles and

Eq. (7) can be used to estimate h_c. Sample cross-sections measured with the SEM yielded a contact angle of $\theta = 83° \pm 8°$ where the uncertainties are 95% confidence limits. Examples of the SEM cross sections are shown in Fig. 4. The contact angle complies with the principles of dewetting phenomena: $\theta < 90°$ [37,43,44]. The estimates of relevant physical parameters are $A = -10^{(-18.25\pm0.09)}$J, $\gamma = 10^{(0.13\pm0.09)}$J/m^2, and $h_c = 10^{(-8.96\pm0.02)}$ m, respectively. These parameters are in good agreement with the expected range of A between -10^{-18} and -10^{-21} J and the literature value of $\gamma \approx 10^{0.18}$ J/m^2 [20,22]. The value determined for h_c is approximately five atomic Pd layers.

4. Discussion

Agreement between the experimental observations, the Gaussian random field behaviors predicted by Minkowski functionals, and the spatial ordering predicted by the free energy theoretical framework, demonstrate that Pd dewets from SiN via spinodal instabilities. Notably, this behavior occurred at T = 800 K, well below the melting point of Pd (1825 K). This suggests that the high temperatures provided by laser heating are not required for spinodal dewetting and that the liquid state may not be necessary to take advantage of the unique self-assembly and ordering that spinodal dewetting provides. The results presented show that spinodal dewetting of high-melting point metals is practical for high-throughput fabrication of metal nanostructures and rapid optimization of their unique properties.

If the metal is not in the liquid state during the spinodal dewetting process observed in this study, the mechanisms for atomic movement at these conditions should be considered. In the case of solid-state materials, alternative mechanisms include surface evaporation and surface diffusion. These processes were shown to be relevant in the context of thermal grooving, whereby a hole is nucleated at a cleft defect/grain boundary and the deepening of crevices results in the effective dewetting of the metal film from a substrate [18]. Nonetheless, surface evaporation and surface diffusion are not dependent on h_0 and do not promote spontaneous roughening of the surface, but rather smoothening. Furthermore, the spatial configuration of nucleated holes is likely due to the location of defects or grain boundaries that are present prior to any perturbation of the system by annealing. The evolution of the Pd thin film observed in this study likely has a contribution from the solid state transport mechanisms driven by surface tension, and the interfacial potential free energy. The role that each possible process imparts in this system will be dependent on many factors. One relevant factor is the effect that the nanoscale dimensions have on material properties of the thin film system. For example, it is known that nanoscale depression of the melting point occurs as the ratio of surface to bulk atoms increases and the net cohesive energy decreases. The melting point depression also depends on the shape and curvature of the material surface [45–47]. The uncertainty in the melting point depression also directly impacts estimates of the surface tension [48]. While this uncertainty is currently problematic, the methodology presented here is suited for elucidating this thermophysical quantity.

From the standpoint of technological advancement and scientific understanding of thin continuous and nanoparticulate films, our approach has significant potential impact. For example, using a single sample with a structural gradient induced by dewetting from a thickness gradient, one could quickly tune and optimize particle spacing, size, and shape for plasmon-enhanced light scattering in next generation photovoltaic cells. Catalysts can be compared on a variety of supports to optimize activity, increase longevity, minimize sintering, and determine whether the support plays an active role. Ideally, to obtain smaller error limits and greater certainty, these pursuits will require a library with a greater range of initial thicknesses and resulting structures. Therefore, instead of using smaller step increments, a better approach would be to use a continuous thickness gradient across the sample. Most applications of metallic nanoparticles benefit from the use of alloys rather than pure metals. Our approach allows simultaneous analysis of both structural and compositional degrees of freedom by creating gradients in both thickness and composition on perpendicular directions lateral to the film. This will allow a library of sensitivity-structure–composition relationships to be determined rapidly and in a straightforward manner. There are no reports of work that has combined these degrees of freedom simultaneously. The method presented is also scalable and can be applied to larger substrates with much more complex morphologies than a flat surface.

5. Conclusion

In the past, spinodal dewetting has largely been considered a phenomenon isolated to polymer and liquid films. However, recent reports have shown that metallic thin films can also exhibit spinodal dewetting behavior. This has opened a door to accelerated discovery of supported metal systems, with precisely controlled structures, tuned to obtain optimal performance for various applications. With the reported development of a method that exploits heat transfer by conduction rather than the previously used pulsed-laser heating technique to dewet the metals, understanding structure-sensitivity of nanostructure metal particles over a broad range of applications is possible.

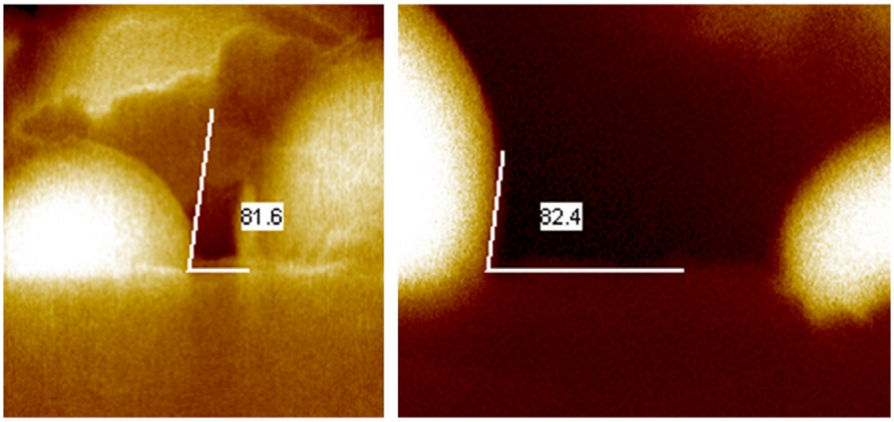

Fig. 4. Scanning tunneling microscopy images of cross sections through Pd structures following dewetting from the silicon nitride surface. These have been used to measure the contact angles between the dewetted Pd features and the exposed substrate surface.

Acknowledgments

This technical effort was performed in support of the National Energy Technology Laboratory's on-going research in Computational and Basic Sciences under the RDS contract DE-AC26-04NT41817 and RES contract DE-FE0004000. WDM would like to thank J. Schneider for using his AFM, as well as M. Reichert, B. Howard, and P. Ohodnicki for their help with materials analysis.

References

[1] Y. Lee, K. Koh, H. Na, K. Kim, J.J. Kang, J. Kim, Nanoscale Res. Lett. 4 (2009) 364.
[2] M. Quinten, A. Leitner, J.R. Krenn, F.R. Aussenegg, Opt. Lett. 23 (1998) 1331.
[3] M.L. Brongersma, J.W. Hartman, H.A. Atwater, Phys. Rev. B 62 (2000) 16356.
[4] I. Lazic, P. Klaver, B. Thijsse, Phys. Rev. B 81 (2010) 13.
[5] S.H. Sun, C.B. Murray, D. Weller, L. Folks, A. Moser, Science 287 (2000) 1989.
[6] J.M. Nam, C.S. Thaxton, C.A. Mirkin, Science 301 (2003) 1884.
[7] J.N. Anker, W.P. Hall, O. Lyandres, N.C. Shah, J. Zhao, R.P. Van Duyne, Nat. Mater. 7 (2008) 442.
[8] V.E. Ferry, J.N. Munday, H.A. Atwater, Adv. Mater. 22 (2010) 4794.
[9] M.I. Stockman, Phys. Today 64 (2011) 39.
[10] D.C. Meier, D.W. Goodman, J. Am. Chem. Soc. 126 (2004) 1892.
[11] Y. Nishihata, J. Mizuki, T. Akao, H. Tanaka, M. Uenishi, M. Kimura, T. Okamoto, N. Hamada, Nature 418 (2002) 164.
[12] G.A. Somorjai, H. Frei, J.Y. Park, J. Am. Chem. Soc. 131 (2009) 16589.
[13] J.J. Agresti, E. Antipov, A.R. Abate, K. Ahn, A.C. Rowat, J.C. Baret, M. Marquez, A.M. Klibanov, A.D. Griffiths, D.A. Weitz, Proc. Natl. Acad. Sci. U. S. A. 107 (2010) 4004.
[14] J. Kononen, L. Bubendorf, A. Kallioniemi, M. Barlund, P. Schraml, S. Leighton, J. Torhorst, M.J. Mihatsch, G. Sauter, O.P. Kallioniemi, Nat. Med. 4 (1998) 844.
[15] J.C. Meredith, A.P. Smith, A. Karim, E.J. Amis, Macromolecules 33 (2000) 9747.
[16] S.M. Senkan, Nature 394 (1998) 350.
[17] X.D. Xiang, X.D. Sun, G. Briceno, Y.L. Lou, K.A. Wang, H.Y. Chang, W.G. Wallacefreedman, S.W. Chen, P.G. Schultz, Science 268 (1995) 1738.
[18] W.W. Mullins, J. Appl. Phys. 28 (1957) 333.
[19] E.J. Luber, B.C. Olsen, C. Ophus, D. Mitlin, Phys. Rev. B 82 (2010) 085407.
[20] R. Seemann, S. Herminghaus, K. Jacobs, Phys. Rev. Lett. 86 (2001) 5534.
[21] J. Trice, D. Thomas, C. Favazza, R. Sureshkumar, R. Kalyanaraman, Phys. Rev. B 75 (2007) 235439.
[22] H. Krishna, R. Sachan, J. Strader, C. Favazza, M. Khenner, R. Kalyanaraman, Nanotechnology 21 (2010) 1.
[23] A. Sharma, Eur. Phys. J. E 12 (2003) 397.
[24] A. Vrij, Discuss. Faraday Soc. 42 (1966) 23.
[25] J. Sarkar, A. Sharma, Langmuir 26 (2010) 8464.
[26] U. Thiele, A.M. Jonas, A. Sharma, H. Kaya, B. Jerome, A.M. Jonas, Eur. Phys. J. E 12 (2003) 395.
[27] J. Bischof, D. Scherer, S. Herminghaus, P. Leiderer, Phys. Rev. Lett. 77 (1996) 1536.
[28] S. Herminghaus, K. Jacobs, K. Mecke, J. Bischof, A. Fery, M. Ibn-Elhaj, S. Schlagowski, Science 282 (1998) 916.
[29] J. Trice, C. Favazza, D. Thomas, H. Garcia, R. Kalyanaraman, R. Sureshkumar, Phys. Rev. Lett. 101 (2008) 017802.
[30] S. Strobel, C. Kirkendall, J.B. Chang, K.K. Berggren, Nanotechnology 21 (2010) 505301.
[31] J. Becker, G. Grun, R. Seemann, H. Mantz, K. Jacobs, K.R. Mecke, R. Blossey, Nat. Mater. 2 (2003) 59.
[32] H. Mantz, K. Jacobs, K. Mecke, J. Stat. Mech.: Theory Exp. 12 (2008) 12015.
[33] R. Khanna, N.K. Agnihotri, M. Vashishtha, A. Sharma, P.K. Jaiswal, S. Puri, Phys. Rev. E 82 (2010) 011601.
[34] G. Reiter, A. Sharma, A. Casoli, M.O. David, R. Khanna, P. Auroy, Langmuir 15 (1999) 2551.
[35] J.W. Cahn, Am. Ceram. Soc. Bull. 44 (1965) 307.
[36] A. Vrij, J.T. Overbeek, J. Am. Chem. Soc. 90 (1968) 3074.
[37] V.S. Mitlin, Colloids Surf. A 89 (1994) 97.
[38] E. Ruckenstein, R.K. Jain, J. Chem. Soc. Faraday Trans. 2 (70) (1974) 132.
[39] V.S. Mitlin, J. Colloid Interface Sci. 156 (1993) 491.
[40] H. Krishna, C. Favazza, A.K. Gangopadhyay, R. Kalyanaraman, JOM 60 (9) (2008) 37.
[41] S. Herminghaus, Phys. Rev. Lett. 83 (12) (1999) 2359.
[42] H. Krishna, N. Shirato, C. Favazza, R. Kalyanaraman, Phys. Chem. Chem. Phys. 11 (37) (2009) 8136.
[43] N.V. Churaev, V.D. Sobolev, Adv. Colloid Interface Sci. 61 (1995) 1.
[44] N.V. Churaev, Adv. Colloid Interface Sci. 58 (2–3) (1995) 87.
[45] Y.F. Zhu, J.S. Lian, Q. Jiang, J. Phys. Chem. C 113 (39) (2009) 16896.
[46] Z. Zhang, J.C. Li, Q. Jiang, J. Phys. D: Appl. Phys. 33 (20) (2000) 2653.
[47] K.K. Nanda, S.N. Sahu, S.N. Behera, Phys. Rev. A 66 (1) (2002) 013208.
[48] T. Iida, R. Guthrie, M. Isac, N. Tripathi, Metall. Mater. Trans. B 37 (3) (2006) 403.